

# Creep Behavior of a High- $\gamma'$ Ni-Based Superalloy Fabricated *via* Electron Beam Melting



PATXI FERNANDEZ-ZELAIA, OBED D. ACEVEDO, MICHAEL M. KIRKA, DONOVAN LEONARD, SEAN YODER, and YOUSUB LEE

Additive manufacturing enables the fabrication of complex engineering components previously inaccessible through traditional processes. Nickel-base superalloys with large  $\gamma'$  volume fraction are typically considered non-weldable and therefore exhibit a propensity for cracking during the fusion process. These crack-prone materials, however, are of great importance in gas turbine engines due to their excellent high temperature creep resistance. In this study we investigate the creep behavior of IN738LC produced by the electron beam melting process. We find that with appropriate post-build heat treatment the creep response of material oriented in the build direction exhibits deformation and rupture behavior comparable to that of conventionally cast IN738 & IN738LC. In the transverse direction properties fall below the expected cast behavior, however, we argue this is likely due to differences in grain scale and crystallographic texture. It may be possible to coarsen the grain morphology with appropriate process-parameter optimization in order to reduce the severity of intergranular fracture in the transverse direction. These results illustrate that high temperature properties exhibited by additively manufactured IN738LC are suitable for the hot section of gas turbine engines.

<https://doi.org/10.1007/s11661-020-06095-3>

© The Minerals, Metals & Materials Society and ASM International 2021

## I. INTRODUCTION

THE efficiency of land based gas turbine engines is closely related to the maximum engine operating temperature.<sup>[1–4]</sup> Consequently, improvements in efficiency have historically followed the development of increasingly temperature-resilient nickel-base (Ni-base)

superalloys.<sup>[1–4]</sup> From the first superalloys up to the 1950s blades were utilized in the wrought condition.<sup>[1,2,5]</sup> Cast systems followed which enjoyed improvements in properties due to advances in casting technology.<sup>[1,2]</sup> Through the 1960s and 1970s directional solidification was developed by VerSnyder and others at Pratt & Whitney which enabled manipulation of the meso-scale microstructure.<sup>[6–10]</sup> Naturally, single crystal casting followed which further improved creep behavior.<sup>[6,11–15]</sup> The history of the manufacture and development of these alloys and their impact on creep performance is summarized in Figure 1.

Additive manufacturing (AM), much like casting before it, offers an opportunity for additional innovation in the development of novel gas turbine components. Selective electron beam melting (EBM) as been used for spatial control of local crystallographic orientation in IN718.<sup>[16]</sup> Two recent papers have demonstrated novel scanning strategies for manipulating the grain morphology in IN718 *via* control of the local solidification dynamics.<sup>[17,18]</sup> Several researchers have exploited solidification physics *via* a careful laser rastering strategy to generate periodic columnar “zig-zag” structures from IN718.<sup>[19–21]</sup> Recent works by identified processing conditions which yielded the fabrication of single crystal prismatic geometries with EBM AM.<sup>[22–24]</sup> Laser processing conditions have been identified yielding extremely sharp near-single-crystal textures in IN738LC.<sup>[25]</sup>

---

PATXI FERNANDEZ-ZELAIA is with the Energy & Transportation Science Division, Oak Ridge National Lab, Oak Ridge, TN. Contact e-mail: 3pf@ornl.gov MICHAEL M. KIRKA and DONOVAN LEONARD are with the Materials Science & Technology Division, Oak Ridge National Laboratory, Oak Ridge, TN. OBED D. ACEVEDO is with the The Bredesen Center for Interdisciplinary Research and Graduate Education, University of Tennessee, Knoxville, TN. SEAN YODER is with the Blue Origin, Kent, WA. YOUSUB LEE is with the Computational Sciences & Engineering Division, Oak Ridge National Laboratory, Oak Ridge, TN.

This manuscript has been authored by UT-Battelle, LLC under Contract No. DE-AC05-00OR22725 with the U.S. Department of Energy. The United States Government retains and the publisher, by accepting the article for publication, acknowledges that the United States Government retains a non-exclusive, paid-up, irrevocable, world-wide license to publish or reproduce the published form of this manuscript, or allow others to do so, for United States Government purposes. The Department of Energy will provide public access to these results of federally sponsored research in accordance with the DOE Public Access Plan (<http://energy.gov/downloads/doe-public-access-plan>).

Manuscript submitted March 5, 2020; accepted October 30, 2020.

Article published online January 1, 2021

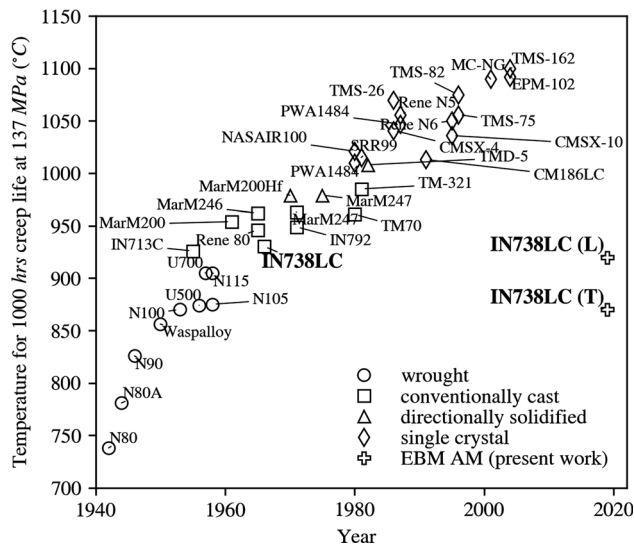


Fig. 1—Historical evolution of superalloy manufacturing and associated creep performance. Figure adapted from original plot found in Ref. [1]. Included are results from this work for historical context.

There is a plethora of additional works in the literature investigating the impact of AM microstructure on mechanical properties.<sup>[26–30]</sup> Through AM processing there is the possibility for even greater control of microstructure in gas turbine engine components. However, defect-free fabrication is made difficult due to a host of potential defect mechanisms.<sup>[31]</sup> High  $\gamma'$  volume fraction alloys, which are desirable due to their enhanced high-temperature creep resistance,<sup>[32,33]</sup> are particularly difficult to print due to a host of potential cracking mechanisms.<sup>[34–40]</sup> Hence, a major current research challenge in the fabrication of high  $\gamma'$  Ni-based superalloys is the identification of suitable process conditions under which printing can achieve defect-free material.

High temperature strength and creep resistance in Ni-based superalloys is owed largely to the ordered (L1)<sub>2</sub> intermetallic  $\gamma'$  precipitates which impede dislocation motion.<sup>[1,2,11,41,42]</sup> The precipitate structure impedes dislocation motion *via* a variety of deformation mechanisms (*e.g.* Orowan looping, precipitate shearing, *etc.*) which are influenced by the imposed rates, temperatures, and stresses.<sup>[1,11,42–44]</sup> Additionally, the structure at higher length scales, for instance the grain morphology and crystallographic texture in directionally solidified (DS) castings, influences the creep response.<sup>[44,45]</sup> A thorough study of DS IN738 to study the orientation dependence of creep over a wide range of temperatures and stresses.<sup>[44]</sup> These authors found that longitudinally oriented samples consistently exhibited higher ductility due to a relative lack of grain boundaries intersecting the sample surface. Interestingly, the authors found that transversely oriented samples consistently exhibited lower rates of deformation with a  $\sim 4\times$  difference at moderate stress-temperature combinations. At high temperatures (982 °C) and low stresses (100 MPa) longitudinally oriented samples exhibited pct 50 higher

rupture life yet at low temperature (762 °C) and high stresses (400 MPa) transversely oriented creep samples exhibited pct 50 higher lives. The effect of loading orientation on CM247LC-DS at 850 °C and 300 to 400 MPa was studied and found that longitudinally oriented samples exhibited lives an order of magnitude longer and creep rates a factor of 2 lower than the transversely oriented samples.<sup>[45]</sup> A number of intermediate oriented samples (30, 45, 60 deg) were also tested and the authors determined that the crystallographic anisotropy played a role in determining creep deformation behavior.

There exist a limited number of works in the literature which address the creep deformation behavior of AM Ni-based superalloys and even fewer consider their rupture behavior. A study on the creep deformation behavior of IN738LC fabricated *via* laser powder bed fusion (L-PBF) found that in samples oriented longitudinally to the build direction the creep resistance was worse than the mean cast behavior but was comparable to the lower scatter band data.<sup>[28,46]</sup> Transversely oriented samples performed substantially worse. L-PBF IN738LC time-dependent deformation has been observed to be driven by grain boundary sliding under certain test conditions.<sup>[47]</sup> Serrated grain boundaries were observed to resist the GBS mechanism which has been confirmed in another work.<sup>[48]</sup> Defect free IN738LC produced *via* L-PBF, using a 1100 °C heated base plate, exhibits properties in the build direction comparable to the cast material when subject to appropriate post build heat treatment.<sup>[49]</sup> Longitudinally oriented tensile samples of IN718 were found to exhibited superior creep deformation resistance at 630 °C and 900 MPa relative to cast and wrought samples following appropriate heat treatment.<sup>[50]</sup> Detailed microscopy revealed a fine subgrain structure and higher fraction of  $\gamma''$  dispersion strengthening was responsible for the improved resistance. However, rupture properties were not reported and it is unclear how this material would perform under high temperature low stress conditions; grain morphology effects are known to be temperature/stress sensitive.<sup>[51]</sup> EBM IN718, following hot isostatic pressing (HIP), exhibited deformation rates and rupture times comparable to wrought material when tested in the build direction at 650 °C.<sup>[52]</sup> Samples tested transverse to the build direction exhibited an order of magnitude or greater reduction in rupture time. Again, however, testing was done at relatively low temperature and virtually one stress level (580 and 600 MPa) and therefore these results are limited to a narrow range of conditions. Recent work on L-PBF IN718 creep behavior found that even after a direct aging heat treatment longitudinal samples only exhibited half the rupture life obtained by conventional materials<sup>[53]</sup> (conventional data in Reference 52); transverse samples an order of magnitude lower life. It is well established that in IN718 appropriate post build heat treatment may be necessary to eliminate deleterious phases (Laves/ $\delta$ ) which significantly improved creep performance.<sup>[54]</sup>

In this work we investigate the creep behavior of IN738LC, a high  $\gamma'$  fraction crack prone Ni-based superalloy, produced *via* EBM AM. We study both the

deformation response of the printed material as well as the rupture characteristics. We compare our findings to previously published relevant works on creep behavior of Ni-based superalloys to study the merits of AM for fabrication of structural components in gas turbine engines.

## II. EXPERIMENTAL METHODS

### A. Electron Beam Melting

Rectangular bars were fabricated using a Arcam Q10+ EBM machine. Samples with the tensile direction acting along the build direction will be referred to as “longitudinal” samples; “transverse” samples with the tensile axis perpendicular to the build direction. Longitudinal samples were machined from fabricated rectangular bars with dimensions 15 mm × 15 mm × 80 mm. Transverse bars necessitated larger as-printed bars with dimensions 80 mm × 15 mm × 80 mm. A 304 stainless-steel start plate of dimensions 150 mm × 150 mm × 10 mm was used. Initially the plate is preheated to 1000 °C and throughout the build each layer is subject to a preheat step prior to melting to maintain this temperature. The IN738LC powder was acquired from Praxair and the corresponding powder chemistry, provided by the supplier, is shown in Table I. The powder was a large diameter EBM blend with 105 μm ± 45 μm size distribution. Commercial Arcam EBM machines employ a number of control parameters and strategies which adjust process parameters based on interactions between component geometry and the resulting local thermal conditions.<sup>[55]</sup> A contour melt theme was utilized where outer surfaces are melted first followed by hatch filling for interior regions. Critical process settings were the hatch spacing (75 μm), speed function (55), layer thickness (50 μm), and reference current (16 mA). The speed function is concordant with speed (higher speed function, higher speed) however there is not a one-to-one mapping as speed may be changed based on the current. The Arcam software performs these operations based on empirical engineering models in an attempt to control the melt pool shape. While this complicates process window identification for new materials, it provides great flexibility and enables the printing of complex geometries. The accelerating voltage is always fixed at 60 kV. A schematic of the build plate and printed bars is shown in Figure 2. 15 mm × 15 mm cross section bars are utilized for longitudinal testing

and 80 mm × 15 mm bars for transverse samples (in the directions illustrated).

All EBM fabricated samples were subsequently treated using hot isostatic pressing (HIP) at 1200 °C and 120 MPa for 240 minutes. This step is effective at eliminating small defects such as gas porosity as well as solution annealing the printed microstructure. HIPing, however, will not remove larger defects such as surface connected cracks and lack of fusion defects. Samples were subsequently aged at 1120 °C for 2 hours and 843 °C for 24 hours to produce a homogenized precipitate structure. No recrystallization was observed following the HIPing and aging heat treatment. This is in agreement with IN738LC processed *via* laser powder bed fusion which exhibited to recrystallization following a 1180 °C heat treatment for several hours.<sup>[56]</sup>

### B. Mechanical Testing

Cylindrical longitudinal creep samples with a gage length of 25.4 mm and diameter 6.35 mm were machined from the heat treated EBM printed bars. Testing was performed in Satec M class creep frames and displacement measurements were obtained using dial gages. Insulated resistance furnaces were utilized to maintain the imposed temperatures. For comparison experimental rupture and secondary creep rate data for IN738/IN738LC was obtained from literature.<sup>[44,57-61]</sup> To compare the disparity between longitudinal and transversely oriented samples results were further compared to available DS cast results for both IN738<sup>[44]</sup> and another Ni-based superalloy, GTD-111.<sup>[62]</sup> GTD-111 was chosen for comparison purposes as the cited work is exhaustive and reports *all* of the relevant results (rates, rupture, and elongation).<sup>[62]</sup> A summary of the available details from these sources is listed in Table II. Note that in Reference 57 the authors do not state the grain size of the cast material utilized for creep testing. However, 1 year earlier the same authors published a paper on fatigue using material procured from the same supplier in the same bar form.<sup>[63]</sup> Therefore, it was assumed that

Table I. IN738LC Powder Chemistry

Cr	Co	Al	Ti	W	Mo	Ta	Nb	B
16.00	8.95	3.34	3.27	2.60	1.74	1.73	0.82	0.009
C	Zr	Fe	Mn	Si	S	Ni		
0.10	0.04	0.11	0.00	0.03	<0.001	bal.		

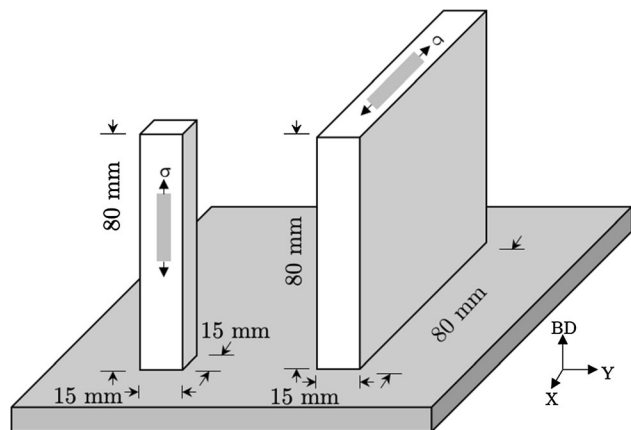


Fig. 2—Schematic of build plate and longitudinal and transverse samples. Tensile direction is in the BD for longitudinal bars and perpendicular to the BD in the transverse bars. Powder is distributed from hoppers by a rake which moved left to right.

it must be the same material used in both studies. In addition, it should be noted that sample sizes and geometries (square vs cylindrical) were used across all studies. This may have some effect but we make no effort here to elucidate on these effects.

### C. Microstructure Characterization

Samples were sectioned using an Allied High Tech TECHCUT 5 and mounted in KonductoMet using a Buehler SimpliMet XPS1. The mounted samples were metallographically prepared using successively finer silica carbide grinding paper and given a final polish with 1  $\mu\text{m}$  diamond on an Allied High Tech MetPrep 4. Samples were etched with Glyceregia to reveal the microstructure. Microscopy was conducted using a Hitachi S4800 field emission scanning electron microscope. Electron back scatter diffraction (EBSD) imaging was performed on a JEOL 6500 field emission scanning electron microscope equipped with a EDAX Hikari camera.

Crystallographic texture illustrations and analysis was generated in the open source software *MTEX*.<sup>[64]</sup>  $\gamma'$  chord length statistics were computed from binarized micrographs using recent algorithms.<sup>[65-67]</sup> Binarizing was performed to identify the  $\gamma'$  phase using standard morphological transformations in the open source image processing library OpenCV.<sup>[68]</sup> Chord length statistics capture the shape and morphology information present in an image which may be used to distinguish between different micrographs. However, extracting physical quantities, particularly in multi-component micrographs, is not straight forward. Therefore, to measure the evolution of the two  $\gamma'$  scales observed in the material particle diameters were measured manually from micrographs.

Metallographically prepared cross-sections were sampled using focused ion beam (FIB) milling for further scanning transmission electron microscopy (STEM) and energy dispersive spectroscopy (EDS) X-ray mapping. FIB lift out was performed with a Hitachi NB5000 FIB/SEM instrument, starting with a  $\sim 500$  nm thick W layer deposited using ion beam induced deposition (IBID) to reduce ‘curtaining’ during the final FIB milling of the specimen. Subsequent thinning of the sample material to electron transparency with the focused ion beam was accomplished using reduced beam currents and accelerating voltages, with final thinning of the metal lamella using 20 kV and  $\sim 1$  pA probe. Scanning transmission electron microscopy (STEM) high angle annular dark field (HAADF), dark field 2 (DF2), dark field 4 (DF4), and bright field (BF) images were collected using a FEI Talos F200X, equipped with a symmetric A-TWIN objective lens integrated with the SuperX energy dispersive spectrometer system and operated at 200 kV. The silicon drift detector (SDD) SuperX system gives the Talos a solid angle of 0.9 sr, maximizing the collection efficiency during X-ray analysis and mapping.

## III. RESULTS

Microstructures for the initial material and various tested materials are shown in Figure 3. The

microstructure initially corresponds to the solutionized and aged state. Aging was performed using the standard heat treatment (SHT) which produces a bimodal precipitate microstructure consisting of  $\sim 1$  and  $\sim 100$  nm  $\gamma'$ . The coarser  $\gamma'$  has a preference for cuboidal morphology. After long exposure it is clear that the precipitate structure coarsens with the disappearance of the finer mode and a change in morphology to spheroidal precipitates. Post-mortem TEM-EDS composition maps in Figure 4 indicate that following testing the metallurgical phases present persist with (Al,Ti)-rich precipitates ( $\gamma'$  formers include Al/Ti/Ta/Nb) and dispersed Cr rich carbides. Interestingly Si-C-N particles were found in all TEM-EDS micrographs. As these samples were produced *via* FIB lift out it is unlikely to be contamination from metallographic preparation. Surprisingly, despite the presence of these particles, the creep response in the longitudinal direction is quite good with respect to the conventionally cast material.

Uniaxial creep results are summarized in Table III. The virgin microstructure prior to testing is shown in Figure 5. The microstructure consists of bimodal  $\gamma'$  and discontinuous grain boundary carbides. It has been argued that these carbides are desirable for high temperature behavior<sup>[69-71]</sup>.

Shown in Figure 6 are the secondary creep strain rate responses corresponding to the tested conditions. A central difference operation was utilized to obtain the strain rate history which were then smoothed using a kernel smoother to eliminate spurious noise. The reported creep rates correspond to the minimum rate observed in the smoothed rate history. Included are results from conventionally cast IN738/IN738LC found in the literature. While comparison against conventionally cast material is difficult due to a lack of exhaustive data under identical conditions these results indicate that longitudinally oriented AM IN738LC behaves similarly to the conventionally cast analogue within experimental uncertainty. The longitudinal 950 °C data passes through the 977 °C cast data. However, given uncertainties associated with the cast data (how values were computed, microstructure/chemistry, *etc.*) we argue that the results are “within the scatter band”. Transversely oriented samples exhibit higher creep strain rates, particularly at low stress levels.

The secondary creep strain rate is commonly expressed using a power-law expression

$$\dot{\epsilon} = A' \exp\left(-\frac{Q}{RT}\right) \sigma^n, \quad [1]$$

where  $A'$  is a constant,  $Q$  the activation energy for creep,  $R$  the universal gas constant,  $T$  temperature,  $\sigma$  the applied uniaxial stress, and  $n$  the rate exponent. The Arrhenius expression is used to capture the temperature dependency of the deformation process. The trend lines shown in Figure 6 correspond to model fit estimates using Eq. [1] The unknown coefficients were estimated independently for longitudinal and transverse orientations using linear regression. These estimated values, as well as values obtained from the literature, are tabulated in Table IV. Note that in some studies only a subset of

Table II. Materials Description

Reference	Material	Fabrication	Tensile Testing	Micro-Structure	Comments
Present Study	IN738LC	EBM, HIP, SHT	25.4 mm gage length 6.35 mm gage diameter	50 to 200 $\mu\text{m}$ grains	L and T tested
60	IN738	SHT	unknown	unknown	—
58, 61	IN738LC	Cast, HIP, SHT new turbine blade	ASTM-E8 samples from blade midsection	unknown	—
57	IN738LC	tensile bar scale casting, SHT	unknown	0.5 mm grains	—
59	IN738	Unknown	unknown	unknown	—
44	IN738	DS cast 100 mm diameter ingots, SHT	76.2 mm length, 31.75 mm gage length, 6.4 mm gage diameter	1 to 2 mm grains	L and T tested
62	GTD-111	DS cast blocks and tensile scale bars	25.4 mm gage length, 4.1 mm gage diameter	1 to 5 mm grains	L and T tested

these values could be estimated as both temperature and applied stress were not varied. For instance if all tests are conducted under the same temperature while varying stress values then the activation energy  $Q$  cannot be estimated. The transition in behavior between low and high stresses is around 250 MPa.<sup>[57]</sup> Here we report the low stress  $n$  and  $Q$  as the majority of our results fall within this range. In the references work the authors utilize a different functional form for the stress-dependence portion of Eq. [1] but an identical Arrhenius term for capturing the temperature dependency and so  $Q$  from this work is included for comparison.<sup>[72]</sup>

In Figure 7 the secondary creep strain rate is shown plotted against the rupture time indicating that the Monkman-Grant hypothesis holds true.<sup>[73]</sup> The Larson-Miller parameter against applied stress is shown in Figure 8 along with results from conventionally cast IN738 and IN738LC for comparison.

To further characterize the grain morphology and crystallographic texture EBSD image maps were obtained from the gage section in planes parallel and perpendicular to the specimen loading direction (Figure 9). All other scans were confirmed to have similar morphology and crystallographic texture. Summary grain size statistics transverse to the columnar/BD are shown in Figure 10. Grains are fairly fine with the distribution resembling an exponential distribution with mean value  $\sim 53 \mu\text{m}$ . In the columnar direction grains are on the order of millimeters in length.

#### IV. DISCUSSION

##### A. Creep Response

The observed secondary creep rate behavior of longitudinally oriented samples, with the AM build direction oriented parallel to the loading direction, is similar to that of conventionally cast IN738/IN738LC. There may be a small debit in terms of creep deformation resistance within a factor of 2 to 3 $\times$ . However, this may very well be considered to be within the scatter band of experimental data. Transverse samples exhibit higher secondary creep strain rates up to an order of magnitude larger than the cast. Similarly, the creep rupture resistance of longitudinally oriented samples is comparable with cast alloys whereas transverse samples yield shorter rupture times; longitudinal samples are within or slightly left of the scatter band whereas transverse samples exhibit a significant debit. The creep deformation response for longitudinal and transverse samples is shown in Figure 11. The transverse sample exhibits far lower ductility and displays a far shorter steady state creep regime.

To the best of our knowledge, only one study on cast IN738/IN738LC reported creep tests of a DS structure in both the longitudinal and transverse directions.<sup>[44]</sup> These authors found that longitudinally oriented samples exhibited better creep ductility yet underwent faster creep deformation. Therefore, effectively, both orientations displayed similar rupture times (ductility exhausted at similar times). Interestingly surface

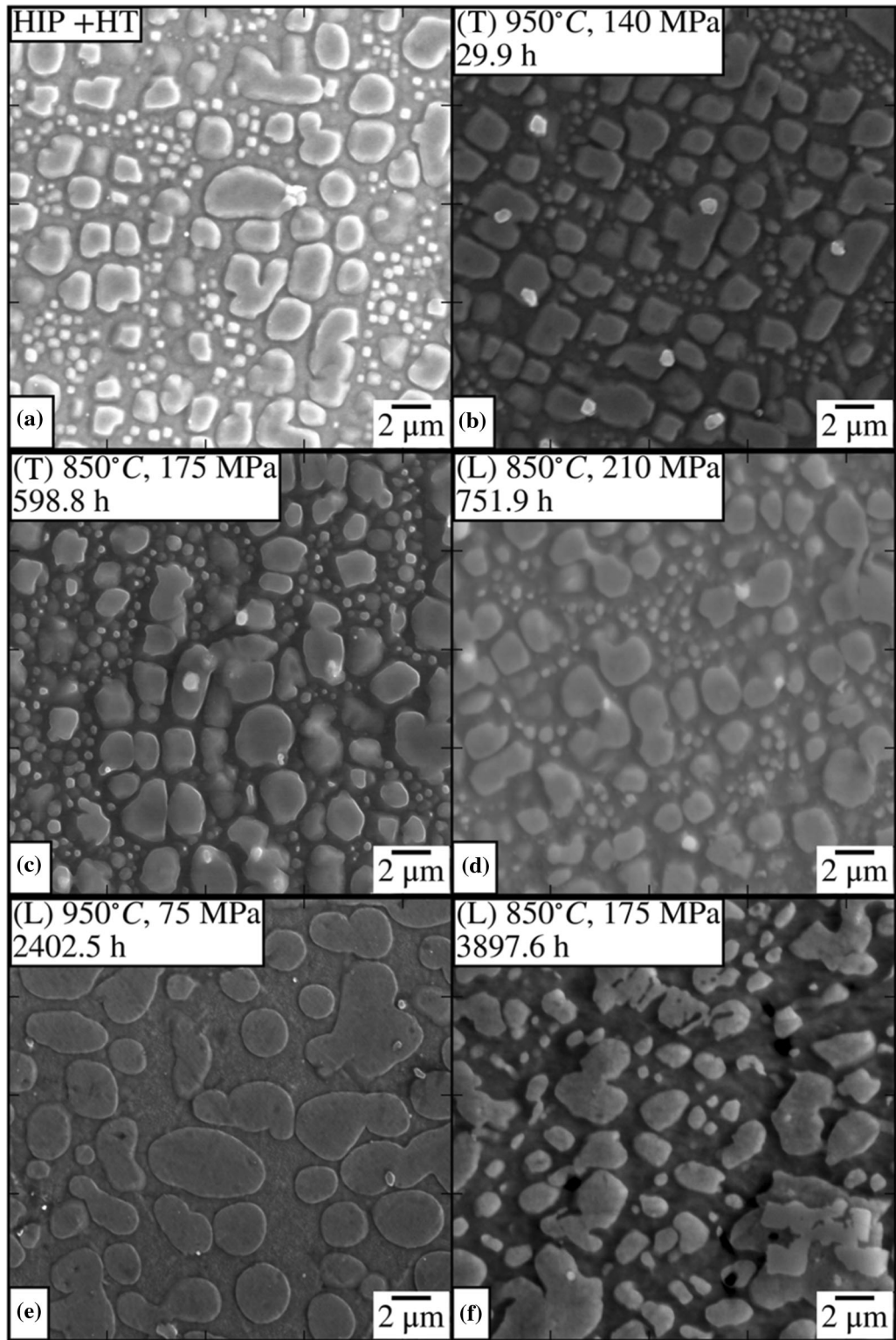


Fig. 3— $\gamma'$  morphology under different test conditions. (a) untested microstructure in HIPed and heat treated conditions (b) through (f) micrographs corresponding to material subject to conditions and times shown in images.

cracking at grain boundaries was more prevalent than cracking at interdendritic regions. The grain size in this work was relatively large on the order of  $\sim 1$  mm. Works on different DS alloy systems indicate that there is a significant disparity between longitudinal and transverse

creep behavior. A study on alloy DS-200 + Hf showed that transverse creep ductility was lower by a factor of two.<sup>[9]</sup> The disparity in rupture behavior, however, was found to be sensitive to testing conditions and failure mechanism. At 750 °C transverse samples exhibited a

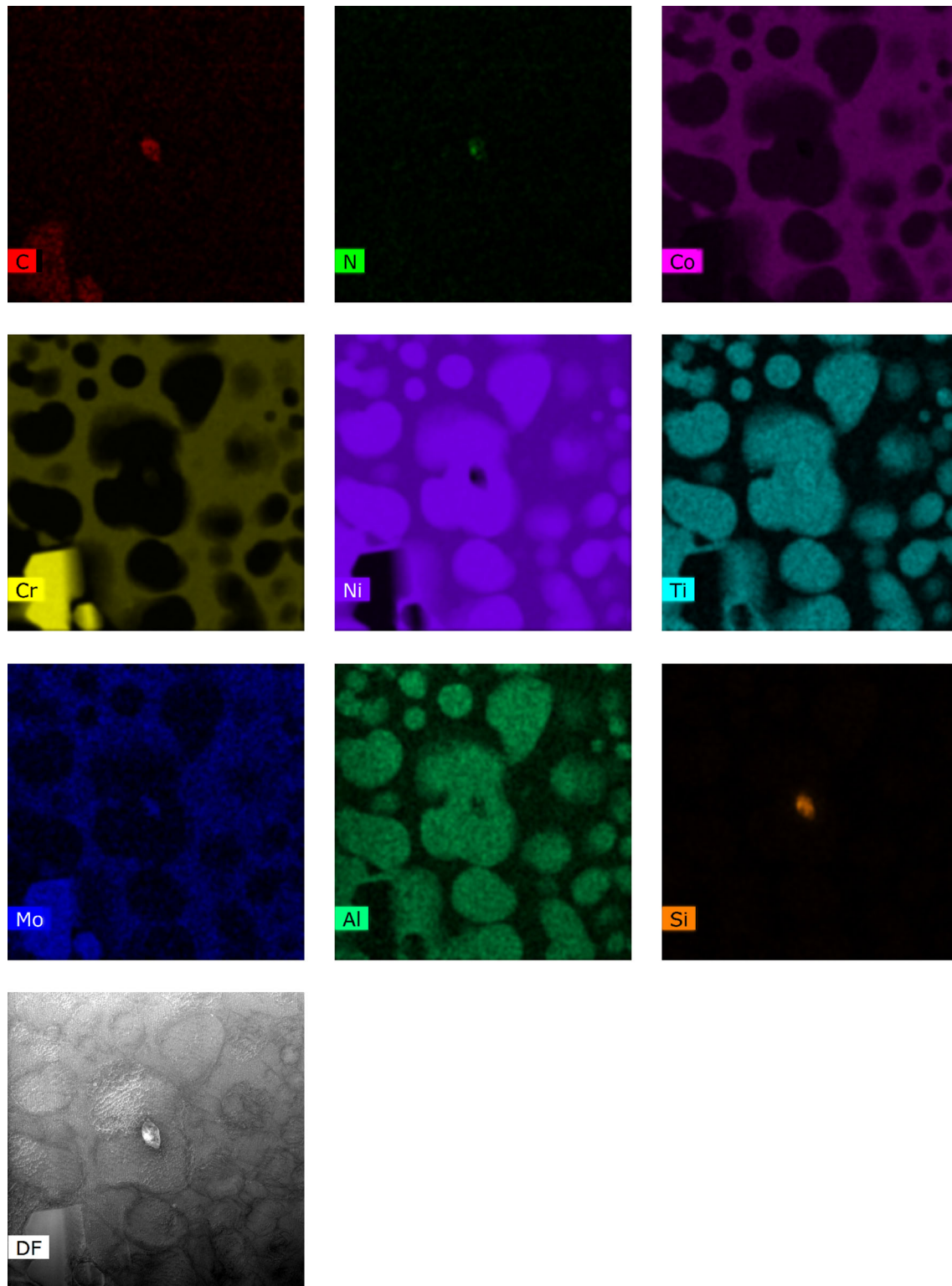


Fig. 4—TEM-EDS concentration maps corresponding to sample tested at 950 °C and 75 MPa ( $t_r = 2402.5$ ).

debit in creep life by up to two orders of magnitude relative to the longitudinal orientation. At 1100 °C, however, this disparity was only a factor of two. Some of the disparity in orientation may further be explained by crystallographic texture effects as it is well established

that the optimal orientation for tensile creep resistance in single crystals is the [001].<sup>[74]</sup>

One cast IN738LC series in Figure 8 does coincide with the transversely oriented AM data. In that work coupons were extracted from the midsection of a virgin

**Table III. IN738LC AM EBM Creep Testing Conditions and Results**

Sample ID	Loading Direction	Temp (°C)	Stress (MPa)	Rupture Time (h)	Rupture Strain ( $\epsilon_f$ )	Secondary Creep Strain Rate ( $s^{-1}$ )
1	L	850	275	227.9	8.3	$4.77 \times 10^{-8}$
3	L	850	240	536.7	9.1	$1.79 \times 10^{-8}$
4	L	850	210	751.9	4.4	$1.00 \times 10^{-8}$
5	L	850	175	3897.6	7.3	$1.79 \times 10^{-9}$
7	L	950	175	45.4	9.6	$3.99 \times 10^{-7}$
11	L	950	140	179.7	9.2	$5.84 \times 10^{-8}$
12	L	950	110	698.8	14.7	$1.44 \times 10^{-8}$
13	L	950	75	2402.5	10.1	$1.83 \times 10^{-9}$
B2-1	T	850	275	43.9	1.4	$9.32 \times 10^{-8}$
B2-2	T	850	240	107.8	1.5	$3.44 \times 10^{-8}$
B2-3	T	850	210	216.8	2.2	$2.12 \times 10^{-8}$
B2-4	T	850	175	598.8	3.4	$9.63 \times 10^{-9}$
B2-5	T	950	140	29.9	4.5	$4.48 \times 10^{-7}$
B2-6	T	950	110	89.7	5.1	$1.36 \times 10^{-7}$
B2-7	T	950	75	299.9	8.0	$4.09 \times 10^{-8}$

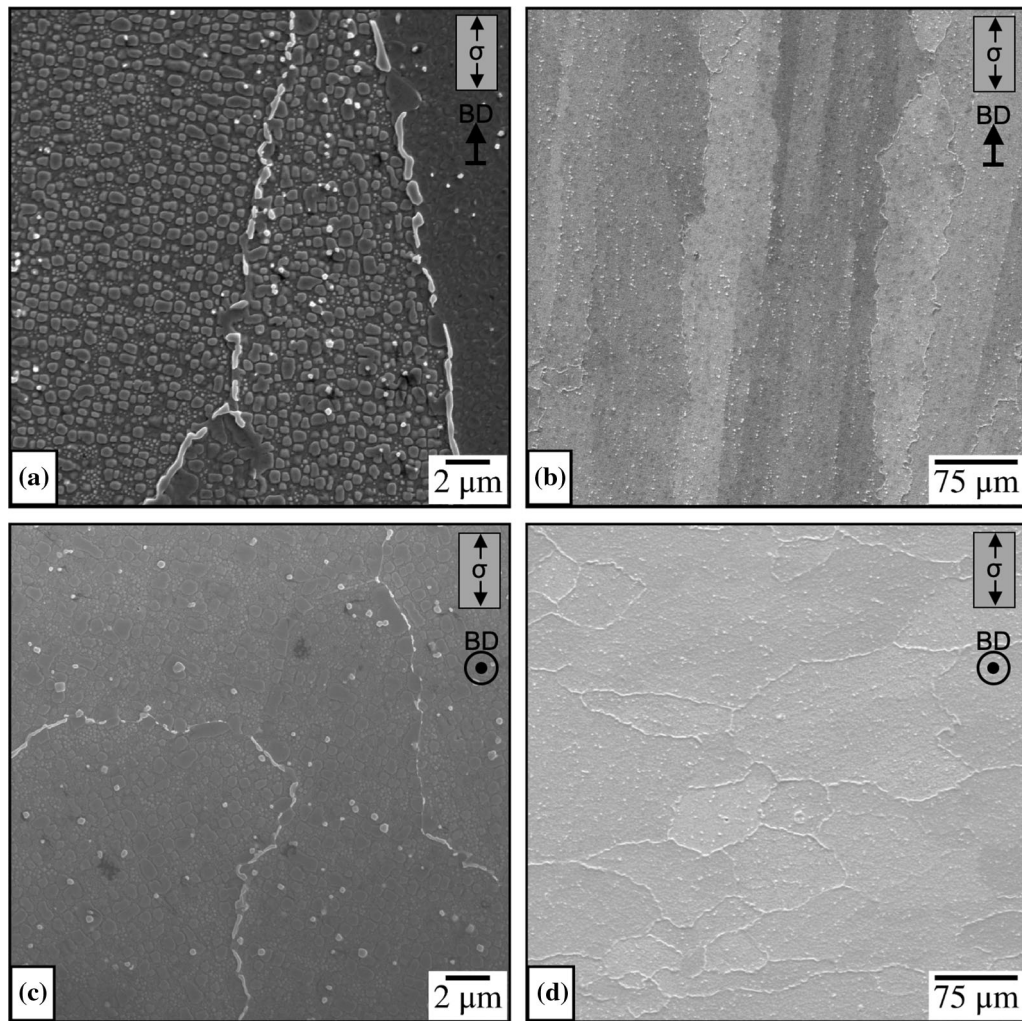


Fig. 5—Virgin microstructure viewed in (a, b) longitudinal orientation with BD vertical and (c, d) transverse orientation with BD out of page. High magnification images reveal bimodal  $\gamma'$  structure and discontinuous grain boundary carbides while low magnification highlights prevalence of grain boundary carbides.



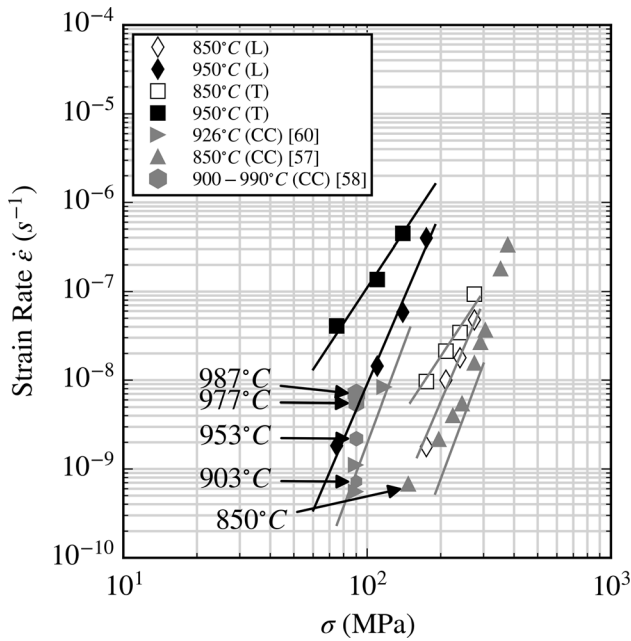


Fig. 6—Steady-state creep response under the tested conditions. Included are results on conventionally cast IN738 & IN738LC.

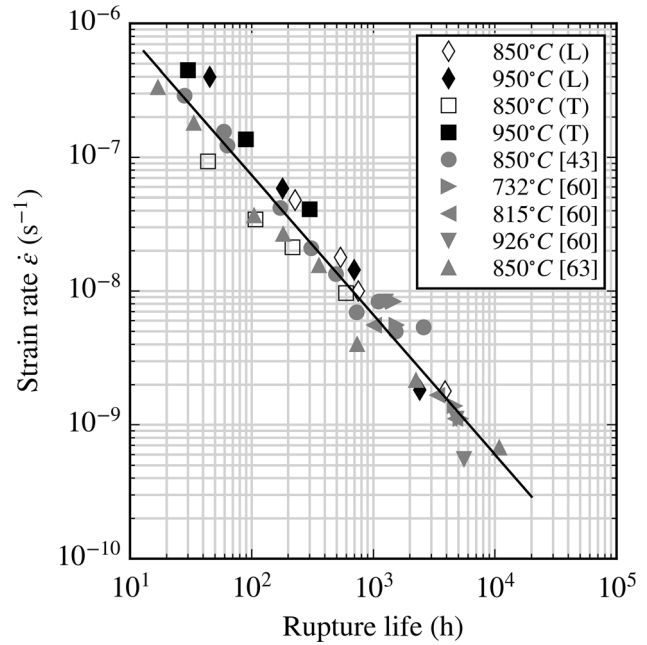


Fig. 7—Monkman–Grant relation between secondary creep strain rate and creep rupture for both AM and cast materials.

Table IV. Power-Law Regression Results

Orientation	$A'$ ( $s^{-1}$ )	$n$	$Q$ (kJ/mol)	Source
EBM. Long.	$9.8 \times 10^{-24}$	6.4	560	current work
EBM. Trans.	$4.8 \times 10^{-18}$	4.2	534	current work
Cast IN738	$7.5 \times 10^{-27}$	7.4	592	60
Cast IN738	$3.4 \times 10^{-26}$	4.1	420	57
Cast IN738LC	—	6.5	—	43
Cast IN738LC	—	—	460	72

cast turbine blade.<sup>[58]</sup> The blade was HIPed after casting followed by a solution annealing and aging heat treatment. Since the remaining cast IN738/IN738LC studies utilized laboratory scale cast ingots and bars, we speculate that the disparity must come from local microstructural variations present in the cast component. Local solidification conditions driven by the thermal gradient will vastly differ in a complex component compared to a cast ingot which introduces some uncertainty regarding the grain structure and texture from Reference 58.

To compare the disparity between longitudinally and transversely oriented samples the ratio of rupture time, elongation at failure, and steady state creep strain rate are shown in Figure 12. For comparison results from an exhaustive work on another high  $\gamma'$  Ni-based superalloy, GTD-111, is shown in Reference 62. We could not find suitable studies on IN738 or IN738LC which included such detailed paired L-T results.

The GTD-111 anisotropic deformation behavior is generally very different than the observed behavior of AM IN738LC. The IN738LC transverse orientation consistently exhibits higher creep strain rates

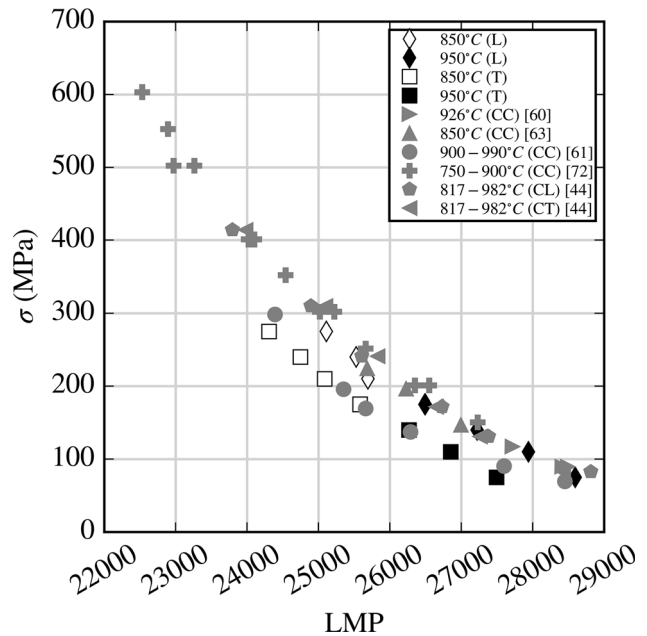


Fig. 8—Creep rupture results. Included are results on conventionally cast IN738 & IN738LC.

( $\dot{\epsilon}_{ss,L}/\dot{\epsilon}_{ss,T} < 1$ ) whereas, with a few exceptions, GTD-111 displays higher rates in the longitudinal orientation ( $\dot{\epsilon}_{ss,L}/\dot{\epsilon}_{ss,T} > 1$ ). This is similar to the prior discussed cast IN738 study which observed larger creep strain rates in the longitudinal direction.<sup>[44]</sup> However, it should be noted that the GTD-111 study utilized three distinct batches of material and the authors noted that creep behavior varied somewhat across each batch.<sup>[62]</sup> Therefore, there is some systematic obfuscation of

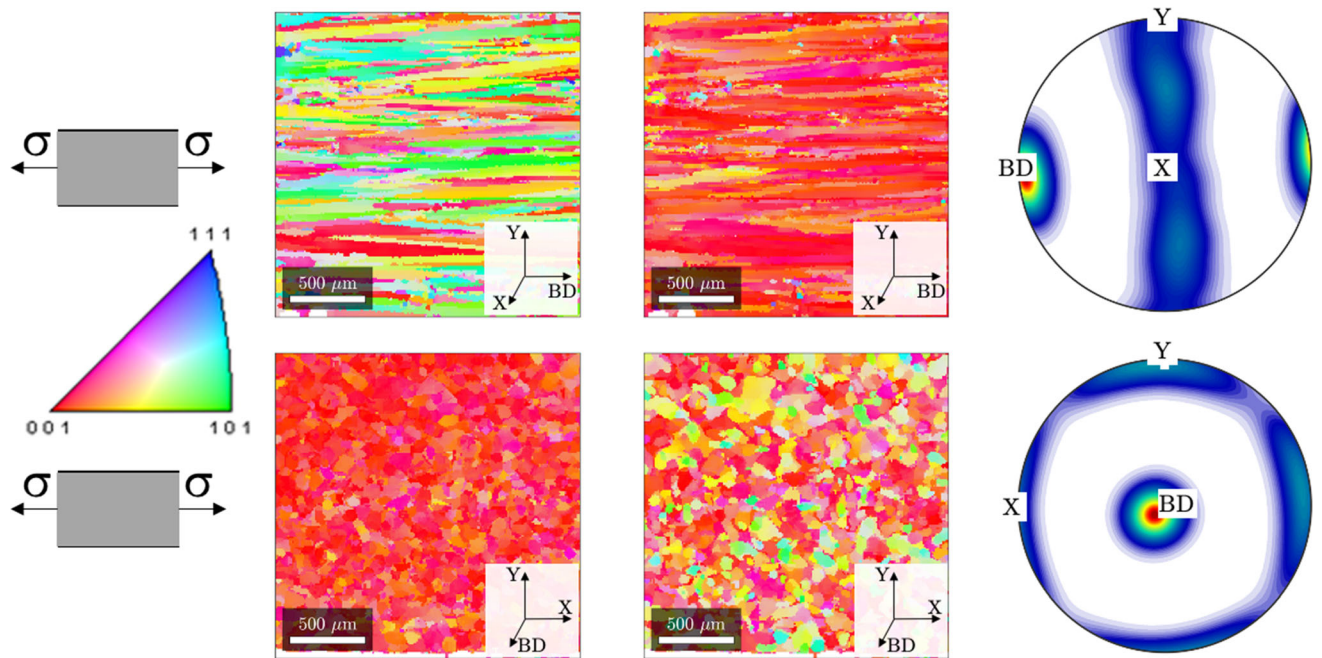


Fig. 9—IPF maps and PF for (top) longitudinal and (bottom) transversely oriented tensile bars. Tensile load direction is horizontal as indicated by  $\sigma$ . Untested HIPed and aged condition.

trends in the GTD-111 data. Nonetheless, the AM IN738LC material consistently exhibits significantly higher creep strain rates in the transverse whereas this is not the case in GTD-111. We attribute this behavior to the disparity in grain morphology between the two systems. It is well established that diffusion is a thermally activated process which is assisted by the presence of grain boundaries.<sup>[75]</sup> This is especially true at low stress values where the disparity in AM IN738LC was observed to be the greatest ( $\dot{\epsilon}_{ss,L}/\dot{\epsilon}_{ss,T} \ll 1$ ). The AM material consists of narrow columnar grains with widths on the order of  $\sim 50$  to  $200 \mu\text{m}$  (Figure 9) whereas GTD-111 consists of  $\sim 1$  mm scale grains. Furthermore, the relatively continuous nature of the IN738LC trends is likely due to the material in the gage section being much larger than the required (RVE) size needed to obtain a homogenized response. The GTD-111 sample gage sections contain only a few grains which contributes to the larger degree of scatter observed in Figure 12.

It is interesting to note that both studies on cast DS GTD-111<sup>[62]</sup> and cast IN738<sup>[44]</sup> observed that the longitudinal direction produced larger minimum creep strain rates. In both casting and AM the preferred growth direction for FCC systems is the [001] direction so we expect that the texture of longitudinal cast and longitudinal AM tensile samples to be similar (neglecting RVE effects). Therefore, the creep behavior of these different systems is likely driven by a competition between crystallographic and grain boundary effects. For the process settings used in this work relatively narrow columnar grains were produced during EBM which may enable Coble creep.<sup>[75]</sup> Recent works have argued that grain boundary sliding occurs under certain conditions during time dependent deformation of

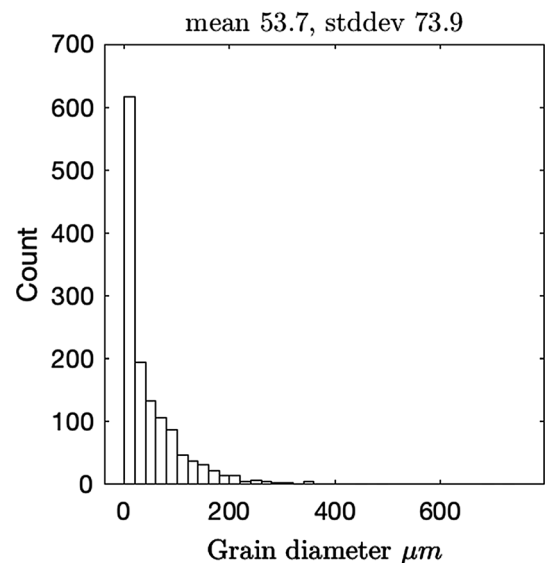


Fig. 10—Grain size statistics from transverse cross section.

L-PBF IN738LC.<sup>[47]</sup> Other works have also shown that serrated grain boundaries can contribute to improved creep performance in superalloys.<sup>[48]</sup> Note that there are studies which show that the meso-scale grain structure may be further manipulated by careful control of the thermal response to produce large columnar grains.<sup>[18]</sup> Therefore, it may be possible to generate coarser grain microstructures which would reduce the number of grain boundaries present in transversely oriented samples and improve rupture behavior. However, in the

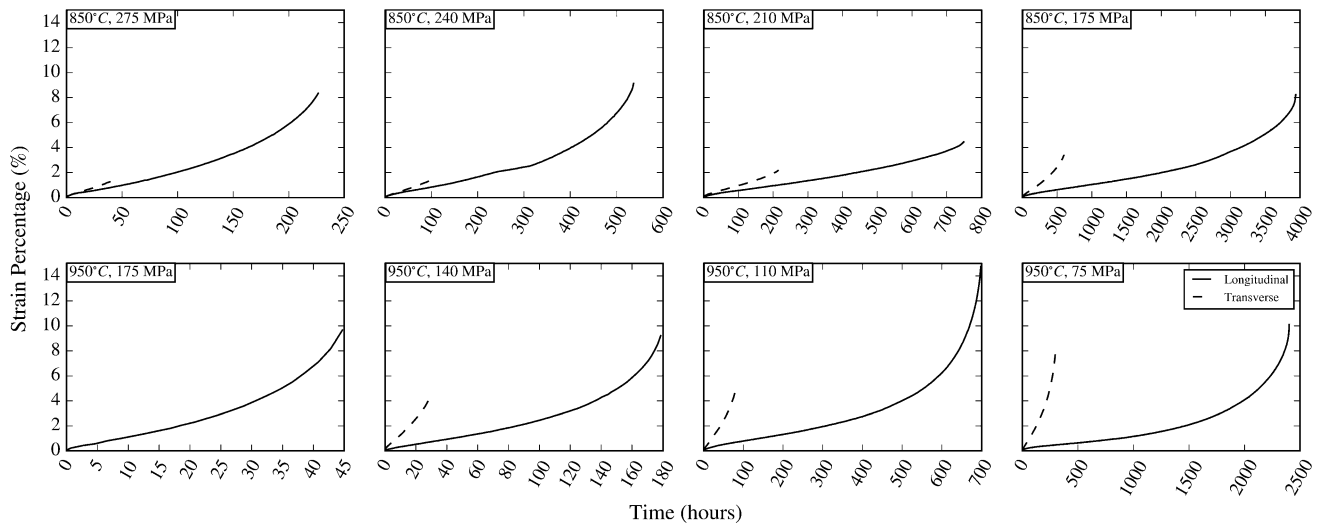


Fig. 11—Creep deformation response for longitudinal and transverse samples.

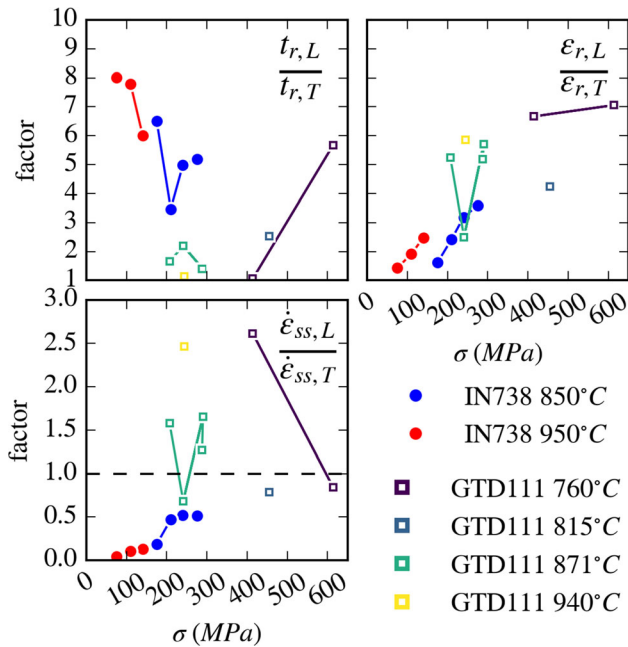


Fig. 12—Comparison of rupture time, elongation at failure, and steady state creep strain rate between longitudinal and transverse loading orientations for AM IN738LC and cast DS GTD-111.<sup>[62]</sup>

referenced work microstructure control was demonstrated for a relatively weldable IN718. In IN738 engineering the grain morphology while mitigating against cracks will be significantly more challenging.

In both studies longitudinal samples yield longer rupture times and exhibit higher ductility. However, the degree of these effects varies between the two systems. The ductility of longitudinally oriented GTD-111 is 5-6X higher with the AM longitudinal direction exhibiting 2 to 3X higher ductility. Creep ductility is dependent on a number of physical microstructural phenomena

and it is difficult to attribute this observations to any one effect. However, it is worth noting that in GTD-111 it was observed that transgranular fracture was prevalent in the longitudinal orientation with cracks preferring interdendritic areas. In the AM IN738LC system grains are much narrower yielding a much higher volumetric grain boundary density and hence there are additional opportunities for intergranular fracture to occur even in the longitudinal direction. For coarse grain GTD-111 intergranular fracture in the longitudinal orientation is nearly negated due to the large grain size. Fracture surfaces of an AM IN738LC sample at 850 °C and 210 MPa is shown Figure 13. The transverse sample contained features resembling the grain morphology which suggests intergranular fracture.

Micrographs taken from the gage section of both longitudinally and transversely oriented samples are shown in Figure 14. Cracking is predominantly intergranular. Interestingly, in longitudinal samples cracking appears to initiate in clusters of equiaxed grains which appear sporadically throughout the otherwise columnar microstructure. Recent work utilizing three dimensional serial sectioning to characterize EBM IN718 revealed that these equiaxed clusters usually appear above a prior lack of fusion defect.<sup>[76]</sup> Although the lack of fusion defect may be “healed” in subsequent layers due to remelting, the local solidification conditions promote the nucleation of these equiaxed clustered. The columnar structure eventually is recovered following subsequent layer deposition. The performance of the EBM manufactured material could therefore be further improved by coarsening the grain structure and eliminating these equiaxed clusters.

The GTD-111 rupture time is on the order of 2X longer for longitudinal samples with the exception of a single very high stress test. For AM IN738LC longitudinal samples had 4 to 8X longer rupture times relative to the transversely oriented samples. This observation can be explained by considering a ductility exhaustion argument. Longitudinal AM IN738LC exhibits creep

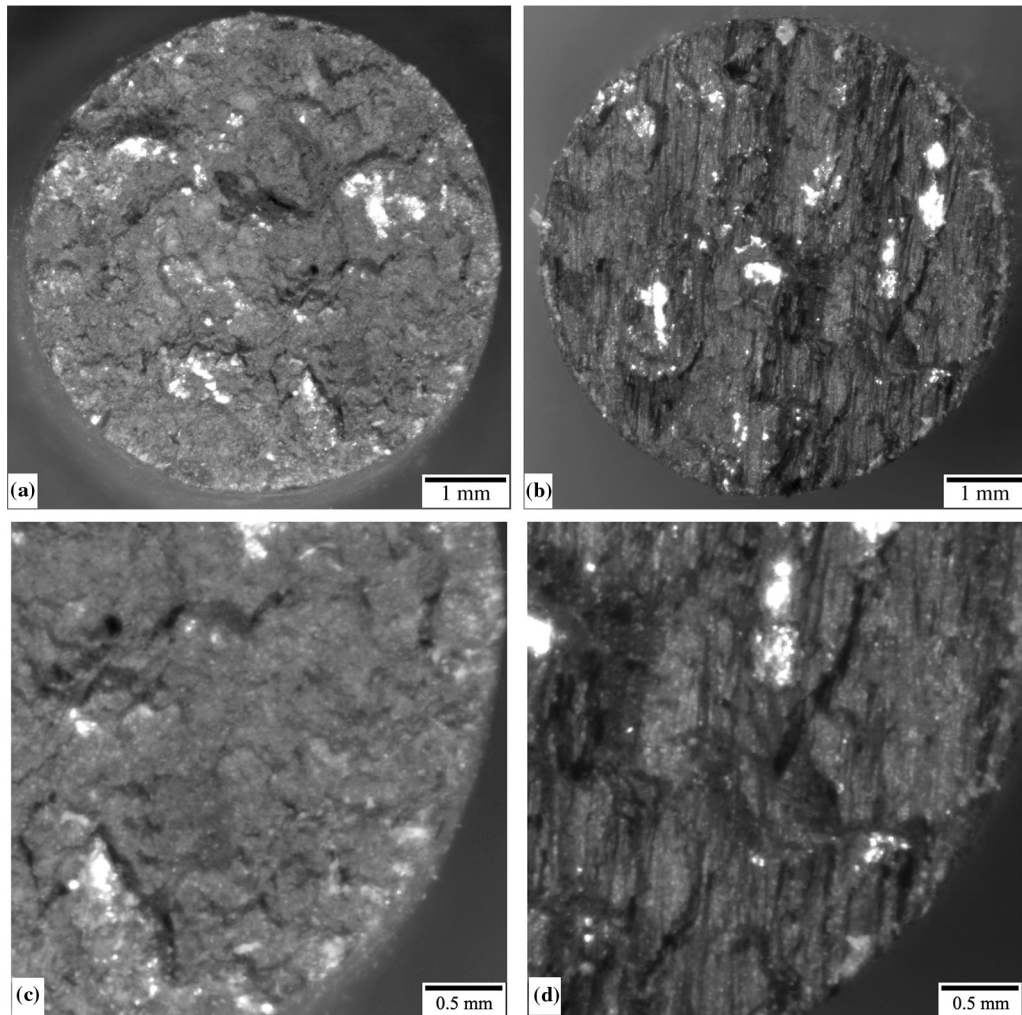


Fig. 13—Fracture surfaces corresponding to 850 °C and 210 MPa for (a) longitudinally oriented samples and (b) transversely oriented sample. (c, d) enlarged views of (a) and (b). Striations in transverse sample indicative of intergranular fracture along columnar grain boundaries.

rates 10 to 50 pct that of the transverse orientation with 2 to 3× better ductility. Hence, overall rupture times are 5 to 10× higher in the longitudinal orientation.

### B. Precipitate Evolution

Untested material, a sample with long rupture time, and sample with short rupture time under different creep test conditions were observed as shown in Figure 15. These images show that carbides were present on the grain boundaries in each condition suggesting that carbides remain stable with no evidence of dissolution. It has been observed in prior works that carbides in in-service turbine blades may evolve subject to exposure to elevated temperatures for very long duration.<sup>[58]</sup> However, this evolution is usually associated with a  $MC \rightarrow M_{23}C_6$  evolution and the presence of carbides

themselves has been observed to be stable up to ~1400 K.<sup>[42]</sup> Additional characterization is necessary to identify the exact structure of carbides observed in both untested and deformed materials.

In Figure 3 the precipitate structure under a select few experimental settings is shown. The initial bimodal microstructure appears to coarsen with a complete disappearance of the secondary  $\gamma'$  phase after sufficient time at high temperature. Summary statistics of both the fine-scale and coarse-scale  $\gamma'$  phase sizes are shown in Figure 16. Measurements were made manually on twenty different precipitates from each micrograph to be able to obtain a simple precipitate scale measurement. There is a clear distinction between fine and coarse bimodal precipitates shown in Figure 3. In the following sections chord length statistics will be utilized to quantify the precipitate morphology distributions.

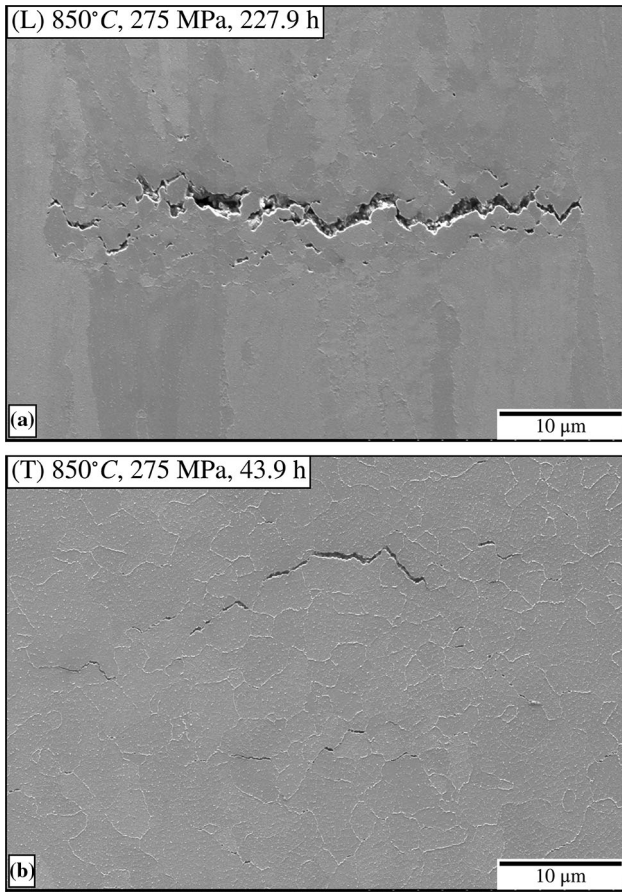


Fig. 14—Micrographs from the gage section of (a) longitudinally oriented sample with the BD vertical and (b) transversely oriented sample with the BD out of the page. Cracking occurs intergranularly in both cases.

While these quantities contain the same information, more interpretation is necessary to extract mean scale quantities.

Rafting is a phenomena observed in many Ni-based superalloys, including IN738,<sup>[77]</sup> where under an applied stress at elevated temperatures the  $\gamma'$  evolves to have a directionally anisotropic morphology.<sup>[1,78–82]</sup> This evolution is driven by the interaction between lattice strain imposed by the applied stress and the intrinsic lattice misfit locally present between  $\gamma$  and  $\gamma'$  phases. Interestingly, no significant rafting was observed and hence results were fit to a cubic-law evolution law which neglects the influence of externally applied stress,<sup>[83]</sup>

$$r^3 - r_0^3 = A' \exp\left(-\frac{Q}{RT}\right), \quad [2]$$

A slight modification is made to introduce a thermally activated Arrhenius term.<sup>[84]</sup> Note that initially the kinetics follow the cubic-law fairly closely with a plateau being reached at longer duration. This is particularly pronounced at 950 °C where initially the microstructure will coarsen across both scales but at larger time scales

the finer scale disappears and the coarser scale growth rate slows. The disappearance of the finer scale, denoted with a dashed trend line, coincides with the plateauing of the coarse scale cubic growth data. This suggests one of two mechanisms; (1) that the larger scale consumes the finer scale at equilibrium and after which growth is impeded when there are few remaining sources of  $\gamma'$  constituents (Ostwald ripening)<sup>[85]</sup> or (2) a non-equilibrium process where the finer scale dissolves into solution faster than it may be consumed by large precipitates.<sup>[86]</sup> Additional work investigating the behavior of this evolution is needed to differentiate between these two possible mechanisms.<sup>[87]</sup>

Alternatively a data-driven strategy may be used to quantify microstructure evolution and identify process-structure trends. Since untested and short exposure microstructures contain a bimodal population of precipitates a scalar value summary statistic, such as mean precipitate size, would be insufficient for describing the observed microstructures. In the physics based approach we circumvent this obstacle by quantifying the two scales separately. A more robust quantification approach is to utilize a more flexible metric such as *angularly resolved chord length statistics*.<sup>[65–67]</sup>

The approach is similar to the ubiquitous line intercept methods (*e.g.* Heyn's method) used in materials science. Rather than reporting a mean chord length statistic, however, a histogram is produced from all measurements and this is repeated at various angles. The value in these metrics is that directional anisotropy, multi-modal size distribution, *etc.* is automatically captured. Algorithms exist for efficient calculation of these quantities directly from images eliminating the need for labor intensive measurements. Furthermore, the method is invariant to feature shape (cubic, spherical, ellipsoidal, *etc.*) in the same way Heyn's intercept method is invariant to such shapes. A few empirically computed distributions are shown in Figure 17.

The difficulty in utilizing these “fingerprint” measurements, however, is that the raw data is inherently multidimensional. Consider that each image processed produces a histogram with 30 bins (*e.g.* frequency of chords of length 5 pixels, 10 pixels, ...) at 20 different angles (*e.g.* chords oriented at 0, 5 deg, ...); this is in effect 600-dimensional data. In order to distill these large, multivariate, descriptions into a few descriptive scalar values principle component analysis (PCA) is used to reduce the dimensionality *via* an orthogonal decomposition. Details can be found in References 65–67 but the idea is to decompose the chord length statistics using a basis representation. This is analogous to a Fourier basis representation of a signal but in PCA the orthogonal basis are computed directly from the data and are not prescribed *a-priori*. This pipeline maps each micrograph to a lower dimensional microstructure statistic space (PCA space) which can be easily visualized. Physical meaning comes from the basis themselves;  $PC_i$  may represent small scale features,  $PC_j$  large scale, and  $PC_k$  anisotropy.

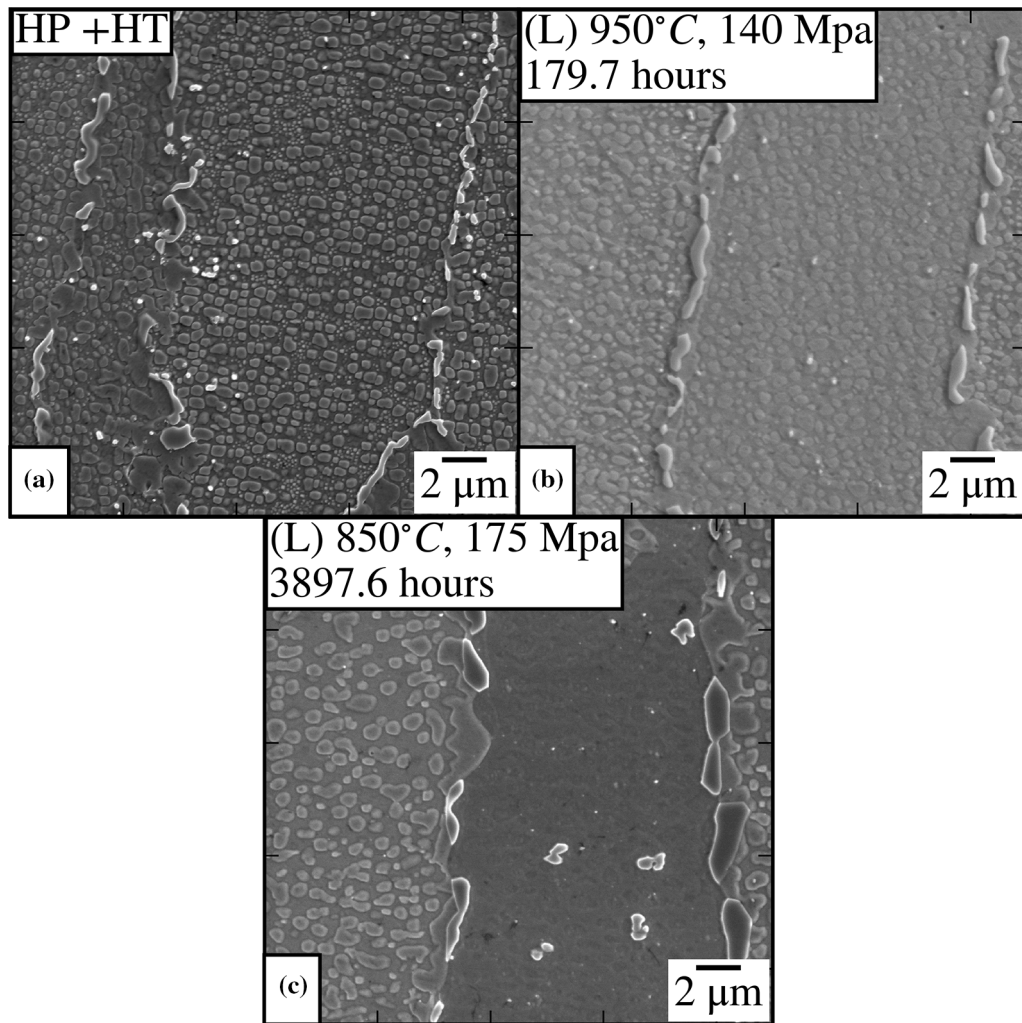


Fig. 15—IN738LC micrographs corresponding to (a) the post processed and heat treated untested material (b) short duration 950 °C microstructure and (c) long duration 850 °C microstructure.

The trends in Figures 17 and 18 agree with the process physics. Initially there is a concentration of density near the origin suggesting that there is a significant fraction of small features (along with larger features at the “tails”). With increasing time the density in the chord length distribution shifts towards larger features. Finally, for 950 °C at sufficiently long times, there is nearly no density left at the smaller length scale features. Interestingly, the data-driven approach correctly captures an overlap between the two tested temperatures which occurs for long duration 850 °C tests and short duration 950 °C tests.

## V. CONCLUSIONS

In this work the creep behavior of EBM AM IN738LC was investigated. Samples oriented in both the transverse and longitudinal directions, relative to the build direction, were tested. Post-mortem microscopy

and fractography was performed to understand the underlying failure mechanisms and microstructure evolution. Results were directly compared to available experimental work on cast IN738/IN738LC to determine the performance of AM fabricated high  $\gamma'$  superalloy materials during high temperature service. The following conclusions were inferred,

- Longitudinally oriented samples display creep resistance and rupture times comparable to the cast material. Amongst the predominantly columnar microstructure sporadic clusters of equiaxed grains were observed and were found to exhibit intergranular cracking not present elsewhere in the microstructure.
- Transversely oriented samples exhibit higher creep rates and decreased rupture strength when compared against longitudinally oriented samples. As cast materials tend to consist of large columnar grains the direct comparisons against available cast data is confounded. However, from the failure analysis it is

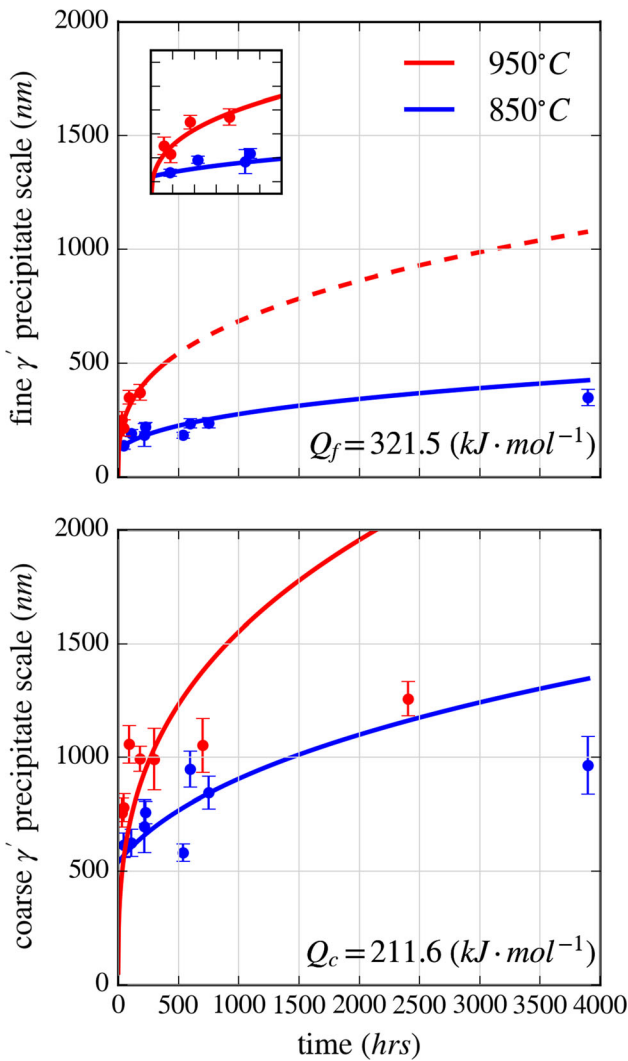


Fig. 16—Observed fine and coarse  $\gamma'$  precipitate size (scale) evolution at both tested temperatures. Trend lines correspond to a cubic-law evolution equation neglecting the effects of applied stress.

believed that the transverse behavior is explained by differences in the meso-scale grain morphology and grain boundary diffusion physics. The orientation of the transverse samples mesoscale structure is deleterious for creep performance; more avenues for diffusion and additional sources for intragranular fracture. Crystallographic texture also likely plays a role as it does in DS and SX materials. EBM process conditions can likely be optimized to mitigate against some of the morphologically driven mechanisms to improve high temperature performance.

- Rafting was not observed in long exposure creep samples. Rather, the  $\gamma'$  morphology coarsened with a transition from cuboidal-spherical bimodal structures to a unimodal coarse spherical structure.
- No significant evolution of the carbides were observed.

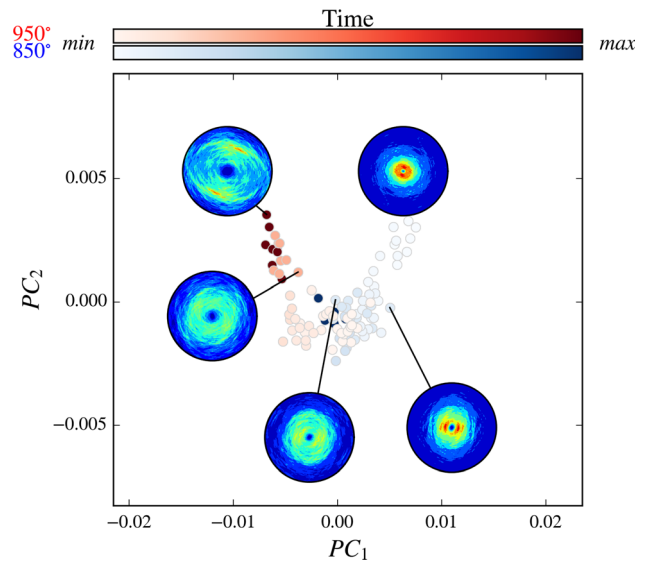


Fig. 17—Computed two-dimensional microstructure space representation and corresponding chord length statistics. Short duration 850 °C micrographs and untested material fall in same space.

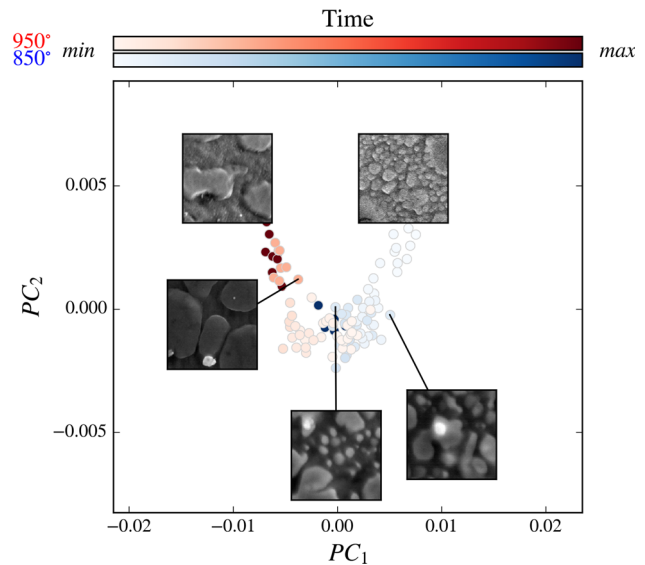


Fig. 18—Computed two-dimensional microstructure space representation and corresponding micrographs. Each micrograph is 2  $\mu\text{m}$  wide. Short duration 850 °C micrographs and untested material fall in same space.

## ACKNOWLEDGMENTS

Research was sponsored by the US Department of Energy, Office of Energy Efficiency and Renewable Energy, Advanced Manufacturing Office, and Office of Fossil Energy, Crosscutting Research Program, under contract DE-AC05-00OR22725 with UT-Battelle LLC and performed in partiality at the Oak Ridge National Laboratory's Manufacturing Demonstration Facility, an Office of Energy Efficiency and Renewable Energy user facility.

## REFERENCES

1. R.C. Reed, *The Superalloys: Fundamentals and Applications*, Cambridge University Press, Cambridge, 2008.
2. C.T. Sims: *Superalloys*, TMS, Warrendale, PA, 1984, pp. 399–419.
3. F. VerSnyder: in *Proceedings of a Conference held in Liege*, 1982.
4. R. Brunetaud, D. Coutouradis, T. Gibbons, Y. Lindblom, D. Meadowcroft, and R. Stickler: in *Proceedings of a Conference held in Liege*, 1982.
5. W. Betteridge and S. Shaw: *Mater. Sci. Technol.*, 1987, vol. 39, pp. 682–94.
6. F.I. Versnyder and M. Shank: *Mater. Sci. Eng.*, 1970, vol. 64, pp. 213–47.
7. B. Pearcey and F. VerSnyder: *J. Aircraft*, 1966, vol. 35, pp. 390–97.
8. S.F.L. Ver: Gas turbine element, US Patent 3,260,505, 1966.
9. L. Mataveli Suave, J. Cormier, P. Villechaise, D. Bertheau, G. Benoit, G. Cailletaud, and L. Marcini: *Mater. High Temp.*, vol. 334–345, 361–71, 2016.
10. J. Lacaze and A. Hazotte: *Text. Microstruct.*, 1970, vol. 13, art. no. 601079.
11. T. Pollock and A. Argon: *Acta Metall. Mater.*, 1992, vol. 401, pp. 1–30.
12. M. Nathal and L. Ebert: *Metall. Trans. A*, 1985, vol. 1610, pp. 1863–70.
13. T. Murakumo, T. Kobayashi, Y. Koizumi, and H. Harada: *Acta Mater.*, 2004, vol. 5212, pp. 3737–44.
14. A. Giamei and D. Anton: *Metall. Trans. A*, 1985, vol. 1611, pp. 1997–2005.
15. P. Caron and T. Khan: *Mater. Sci. Eng.*, 1983, vol. 612, pp. 173–84.
16. R.R. Dehoff, M. Kirka, W. Sames, H. Bilheux, A. Tremsin, L. Lowe, and S. Babu: *Mater. Sci. Technol.*, 2015, vol. 318, pp. 931–38.
17. N. Raghavan, R. Dehoff, S. Pannala, S. Simunovic, M. Kirka, J. Turner, N. Carlson, and S.S. Babu: *Acta Mater.*, 2016, vol. 112, pp. 303–314.
18. N. Raghavan, S. Simunovic, R. Dehoff, A. Plotkowski, J. Turner, M. Kirka, and S. Babu: *Acta Mater.*, 2017, vol. 140, pp. 375–87.
19. G. Dinda, A. Dasgupta, and J. Mazumder: *Scr. Mater.*, 2012, vol. 675, pp. 503–06.
20. H. Wei, J. Mazumder, and T. DebRoy: *Sci. Rep.*, 2015, vol. 5, p. 16446.
21. L.L. Parimi, G. Ravi, D. Clark, and M.M. Attallah: *Mater. Charact.*, 2014, vol. 89, pp. 102–111.
22. C. Körner, M. Ramsperger, C. Meid, D. Bürger, P. Wollgramm, M. Bartsch, and G. Eggeler: *Metall. Mater. Trans. A*, 2018, vol. 499A, pp. 3781–92.
23. M. Ramsperger, R.F. Singer, and C. Körner: *Metall. Mater. Trans. A*, 2016, vol. 473A, 1469–80.
24. E. Chauvet, C. Tassin, J.J. Blandin, R. Dendievel, and G. Martin: *Scr. Mater.*, 2018, vol. 152, pp. 15–19.
25. F. Geiger, K. Kunze, and T. Etter: *Mater. Sci. Eng. A*, 2016, vol. 661, pp. 240–46.
26. V. Popovich, E. Borisov, V.S. Sufiyarov, and A. Popovich: *Met. Sci. Heat Treat.*, 2019, vols. 6011–6012, pp. 701–09.
27. L. Thijs, M.L.M. Sistiaga, R. Wauthle, Q. Xie, J.P. Kruth, and J. Van Humbeeck: *Acta Mater.*, 2013, vol. 6112, pp. 4657–68.
28. K. Kunze, T. Etter, J. Grässlin, and V. Shklover: *Mater. Sci. Eng. A*, 2015, vol. 620, pp. 213–22.
29. T. Etter, K. Kunze, F. Geiger, and H. Meidani: in *IOP Conference Series: Materials Science and Engineering*, vol. 82, p. 012097, IOP Publishing, Bristol, 2015.
30. M.L. Montero-Sistiaga, S. Pourbabak, J. Van Humbeeck, D. Schryvers, and K. Vanmeensel: *Mater. Des.*, 2019, vol. 165, p. 107598.
31. W.J. Sames, F. List, S. Pannala, R.R. Dehoff, and S.S. Babu: *Int. Mater. Rev.*, 2016, vol. 615, pp. 315–60.
32. R.F. Decker: *Metall. Trans.*, 1973, vol. 411, pp. 2495–2518.
33. V. Mohles, D. Rönnpagel, and E. Nembach: *Comput. Mater. Sci.*, 1999, vols. 161–4, pp. 144–50.
34. L.N. Carter, M.M. Attallah, and R.C. Reed: *Superalloys*, 2012, vol. 2012, pp. 577–86.
35. M. Henderson, D. Arrell, R. Larsson, M. Heobel, and G. Marchant: *Sci. Technol. Weld. Join.*, 2004, vol. 91, pp. 13–21.
36. M.J. Donachie and S.J. Donachie: *Superalloys: A Technical Guide*, ASM International, Materials Park, 2002.
37. J. Yang, F. Li, Z. Wang, and X. Zeng: *J. Mater. Process. Technol.*, 2015, vol. 225, pp. 229–39.
38. R. Engeli, T. Etter, S. Hoovel, and K. Wegener: *J. Mater. Process. Technol.*, 2016, vol. 229, pp. 484–91.
39. S. Asavavisithchai, W. Homkrajai, and P. Wangyao: *High Temp. Mater. Processes*, 2010, vols. 291–2, pp. 61–68.
40. O. Ojo, N. Richards, and M. Chaturvedi: *Scr. Mater.*, 2004, vol. 505, pp. 641–46.
41. R. Reed, N. Matan, D. Cox, M. Rist, and C. Rae: *Acta Mater.*, 1999, vol. 4712, pp. 3367–81.
42. R. Stevens and P. Flewitt: *Mater. Sci. Eng.*, 1979, vol. 373, pp. 237–47.
43. R. Stevens and P. Flewitt: *Acta Metall.*, 1981, vol. 295, pp. 867–82.
44. D. Woodford and J. Frawley: *Metall. Trans.*, 1974, vol. 59, pp. 2005–2013.
45. R. Mishra, S. Singh, A. Sriramamurthy, and M. Pandey: *Mater. Sci. Technol.*, 1995, vol. 114, pp. 341–46.
46. L. Rickenbacher, T. Etter, S. Hövel, and K. Wegener: *Rapid Prototyping J.*, 2013, vol. 194, pp. 282–90.
47. J. Xu, H. Gruber, D. Deng, R.L. Peng, and J.J. Moverare: *Acta Mater.*, 2019, vol. 179, pp. 142–57.
48. Y.T. Tang, A.J. Wilkinson, and R.C. Reed: *Metall. Mater. Trans. A*, 2018, vol. 499, pp. 4324–42.
49. J. Risse and C. Broeckmann: *Additive manufacturing of nickel-base superalloy in738lc by laser powder bed fusion*, Tech. Rep, Lehrstuhl für Lasertechnik, 2019.
50. M. Pröbstle, S. Neumeier, J. Hopfenmüller, L. Freund, T. Nien-dorf, D. Schwarze, and M. Göken: *Mater. Sci. Eng. A*, 2016, vol. 674, pp. 299–307.
51. L. Thébaud, P. Villechaise, C. Crozet, A. Devaux, D. Béchet, JM. Franchet, A.L. Rouffié, M. Mills, and J. Cormier: *Mater. Sci. Eng. A*, 2018, vol. 716, pp. 274–83.
52. B. Shassere, D. Greeley, A. Okello, M. Kirka, P. Nandwana, and R. Dehoff: *Metall. Mater. Trans. A*, 2018, vol. 4910A, pp. 5107–117.
53. Y.L. Kuo, S. Horikawa, and K. Kakehi: *Scr. Mater.*, 2017, vol. 129, pp. 74–78.
54. Y.L. Kuo, T. Nagahari, and K. Kakehi: *Materials*, 2018, vol. 116, p. 996.
55. W. Sames: Additive manufacturing of inconel 718 using electron beam melting: processing, post-processing, & mechanical properties, Ph.D. thesis, Texas A & M, 2015.
56. O. Messé, R. Muñoz-Moreno, T. Illston, S. Baker, and H. Stone: *Addit. Manuf.*, 2018, vol. 22, pp. 394–404.
57. G. Jiangting, D. Ranucci, and E. Picco: *Superalloys*, 1984, vol. 1984, pp. 689–98.
58. R. Castillo, A. Koul, and J. Immarigeom: in *Superalloys 1988*, The Metallurgical Society, 1988.
59. National Institute for Materials Science: in *NIMS Creep Data Sheet*, NIMS, Tsukuba, 2007.
60. The International Nickel Company, Inc.: *Alloy IN-738 Technical Data*, The International Nickel Company Inc, New York, 1981.
61. A. Koul, J. Immarigeom, R. Castillo, P. Lowden, and J. Liburdi, in *Proceedings of Superalloys 1988 (Sixth International Symposium)*, pp. 755–764, 1988.
62. A. Ibanez, V. Srinivasan, and A. Saxena: *Fatigue Fract. Eng. Mater. Struct.*, 2006, vol. 2912, pp. 1010–20.
63. G. Jianting, D. Ranucci, and E. Picco: *Mater. Sci. Eng.*, 1983, vol. 581, pp. 127–33.
64. F. Bachmann, R. Hielscher, and H. Schaeben, in *Solid State Phenomenon*, vol. 160, pp. 63–68, Trans Tech Publ, 2010.
65. M.I. Latypov, M. Kühbach, I.J. Beyerlein, J.C. Stinville, L.S. Toth, T.M. Pollock, and S.R. Kalidindi: *Mater. Charact.*, 2018, vol. 145, pp. 671–85.
66. D.M. Turner, S.R. Niezgodna, and S.R. Kalidindi: *Model. Simul. Mater. Sci. Eng.*, 2016, vol. 247, p. 075002.
67. P. Fernandez-Zelaia and S.N. Melkote: *J. Mater. Process. Technol.*, 2019, vol. 273, p. 116251.
68. OpenCV: Open Source Computer Vision Library, 2015.
69. K.A. Unocic, D. Shin, X. Sang, E. Cakmak, and P.F. Tortorelli: *Scr. Mater.*, 2019, vol. 162, pp. 416–20.
70. L. Liu, F. Sommer, and H. Fu: *Scr. Metall. Mater. (U.S.)*, 1994, vol. 30, pp. 587–91.



71. F. Furillo, J. Davidson, J. Tien, and L. Jackman: *Mater. Sci. Eng.*, 1979, vol. 392, pp. 267–73.
72. R. Oruganti, M. Karadge, S. Nalawade, S. Kelekanjeri, and F. Mastromatteo: *Superalloys*, 2012, vol. 2012, pp. 473–79.
73. F.C. Monkman and N. Grant: in *Proceedings of ASTM*, vol. 56, pp. 91–103, 1956.
74. P. Caron, T. Khan, Y. Ohta, and Y. Nakagawa: *Superalloys*, 1988, vol. 1988, pp. 215–24.
75. R. Coble: *J. Appl. Phys.*, 1963, vol. 346, pp. 1679–82.
76. A.T. Polonsky, M.P. Echlin, W.C. Lenthe, R.R. Dehoff, M.M. Kirka, and T.M. Pollock: *Mater. Charact.*, 2018, vol. 143, pp. 171–81.
77. C.S. Kim, C.Y. Hyun, and K.Y. Jhang: *Int. J. Mod. Phys. B*, 2011, vol. 2510, pp. 1385–92.
78. M. Kirka, K. Brindley, R. Neu, S. Antolovich, S. Shinde, and P. Gravett: *Int. J. Fatigue*, 2015, vol. 81, pp. 191–201.
79. M. Kirka, K. Brindley, R. Neu, S. Antolovich, S. Shinde, and P. Gravett: *Int. J. Fatigue*, 2015, vol. 81, pp. 48–60.
80. F.R. Nabarro: *Metall. Mater. Trans. A*, 1996, vol. 273A, pp. 513–30.
81. O. Paris, M. Fa, E. Fa, T. Pollock, P. Fratzl *et al.*: *Acta Mater.*, 1997, vol. 453, pp. 1085–97.
82. N. Matan, D. Cox, C. Rae, and R. Reed: *Acta Mater.*, 1999, vol. 477, pp. 2031–45.
83. R. MacKay and M. Nathal: *Acta Metall. Mater.*, 1990, vol. 386, pp. 993–1005.
84. A. Epishin, T. Link, H. Klingelhöffer, B. Fedelich, and P. Portella: *Mater. High Temp.*, 2010, vol. 271, pp. 53–59.
85. A. Brailsford and P. Wynblatt: *Acta Metall.*, 1979, vol. 273, pp. 489–97.
86. H. Huang, G. Liu, H. Wang, A. Ullah, and B. Hu: *Metall. Mater. Trans. A*, 2020, vol. 513A, pp. 1075–84.
87. I.M. Lifshitz and V.V. Slyozov: *J. Phys. Chem. Solids*, 1961, vols. 191–192, pp. 35–50.

**Publisher's Note** Springer Nature remains neutral with regard to jurisdictional claims in published maps and institutional affiliations.